

# Seismic signature of subduction termination from teleseismic P- and S-wave arrival-time tomography: the case of northern Borneo

Simone Pilia<sup>1</sup>

<sup>1</sup>University of Milan-Bicocca

November 26, 2022

## Abstract

Studies attempting to gain new insights into the last stage of the subduction cycle are typically challenged by limited direct observations owing to a lack of recent post-subduction settings around the world. Central to unravelling how the subduction cycle ends is an understanding of crust and mantle processes that take place after subduction termination. Northern Borneo (Malaysia) represents a unique natural laboratory because it has been the site of two sequential subduction episodes of opposite polarity since the mid-Paleogene. The region exhibits several enigmatic post-subduction (after  $\sim 10$  Ma) features, including: subsidence followed by rapid uplift, localised intraplate volcanism, possible orogen collapse, and a pluton that emerged to become the third highest peak in southeast Asia, Mt Kinabalu (4095 m). Arrival-time residuals from distant earthquake data recorded by the nBOSS seismic network have been used to investigate P- and S-wavespeed variations in the crust and underlying upper mantle beneath northern Borneo. Our 3-D tomographic images consistently show a high-velocity perturbation in western Sabah that we associate with an upper-mantle remnant of the Proto South-China Sea slab, thus providing important constraints for tectonic reconstructions of SE Asia. The tomographic models, combined with other seismological and geological information, reveal evidence for lithospheric removal in eastern Sabah via a drip instability. Our results suggest that lithospheric drips can be smaller than previously thought, yet their effects on the post-subduction evolution of continental lithosphere can be significant.

**Seismic signature of subduction termination from teleseismic P- and  
S-wave arrival-time tomography: the case of northern Borneo**

**Pilia S.<sup>1,2</sup>, Rawlinson N.<sup>1</sup>, Hall R.<sup>3</sup>, Cornwell D.G.<sup>4</sup>, Gilligan A.<sup>4</sup>, Tongkul F.<sup>5</sup>**

<sup>1</sup> Department of Earth Sciences-Bullard Labs, University of Cambridge, Cambridge, UK

<sup>2</sup> Department of Earth and Environmental Sciences, University of Milano-Bicocca, Italy

<sup>3</sup> SE Asia Research Group, Department of Earth Sciences, Royal Holloway University of  
London, Surrey, UK

<sup>4</sup> School of Geosciences, University of Aberdeen, Aberdeen, UK

<sup>5</sup> Faculty of Science and Natural Resources, Universiti Malaysia Sabah, Kota Kinabalu, MY

Corresponding author: Simone Pilia ([simone.pilia@unimib.it](mailto:simone.pilia@unimib.it))



## **Abstract**

Studies attempting to gain new insights into the last stage of the subduction cycle are typically challenged by limited direct observations owing to a lack of recent post-subduction settings around the world. Central to unravelling how the subduction cycle ends is an understanding of crust and mantle processes that take place after subduction termination. Northern Borneo (Malaysia) represents a unique natural laboratory because it has been the site of two sequential subduction episodes of opposite polarity since the mid-Paleogene. The region exhibits several enigmatic post-subduction (after  $\sim 10$  Ma) features, including: subsidence followed by rapid uplift, localised intraplate volcanism, possible orogen collapse, and a pluton that emerged to become the third highest peak in southeast Asia, Mt Kinabalu (4095 m). Arrival-time residuals from distant earthquake data recorded by the nBOSS seismic network have been used to investigate P- and S-wavespeed variations in the crust and underlying upper mantle beneath northern Borneo. Our 3-D tomographic images consistently show a high-velocity perturbation in western Sabah that we associate with an upper-mantle remnant of the Proto South-China Sea slab, thus providing important constraints for tectonic reconstructions of SE Asia. The tomographic models, combined with other seismological and geological information, reveal evidence for lithospheric removal in eastern Sabah via a drip instability. Our results suggest that lithospheric drips can be smaller than previously thought, yet their effects on the post-subduction evolution of continental lithosphere can be significant.

## **1 Introduction**

The recycling of negatively buoyant oceanic lithosphere in a subduction zone has a finite lifespan. Closure of an oceanic basin is a tectonic process deeply embedded in the Wilson Cycle, but reconciling crust and upper-mantle processes with post-subduction surface geology is a challenge. Post-subduction processes are likely to have a profound impact on the way that

continents are built, particularly in regions like the Mediterranean and SE Asia where subduction systems and plate motions operate on a small spatial scale and are generally short-lived. From a geological perspective, the effects of subduction termination on the continents typically leave puzzling and diverse traces in the geological record, such as subsidence followed by uplift, localised intraplate magmatism and exhumation of deeper formations (e.g., Ducea & Saleeby, 1996; Zandt et al., 2004; Levander et al., 2011). A well-studied region where subduction ended in the Miocene is central California, particularly in the southern Sierra Nevada. The geological record indicates southwest migrating subsidence, followed by exhumation and uplift in the Late Miocene (Clark et al., 2005), in addition to a pulse of basaltic volcanism suggesting lower crustal removal and replacement by asthenospheric material in the Pliocene (Ducea and Saleeby, 1996). Passive seismic experiments show a relatively thin crust unable to isostatically compensate 3-4 km of elevation (Wernick et al., 1996; Zandt et al., 2004), and a major high-velocity perturbation located in the upper mantle beneath the southern Great Valley, known as the Isabella anomaly (Raikes, 1980). Various mechanisms have been invoked to explain both geophysical and geological observations, but a widespread consensus has proven to be elusive, with proposed models ranging from i) foundering of a dense lithospheric root developed from the southern Sierra Nevada batholith (Zandt et al., 2004); and ii) the presence of a slab remnant still attached to the Monterey microplate and translating to the east beneath North America (Pikser et al., 2012). A similar set of enigmatic observations have been made for the south-eastern Carpathian region (e.g., Göğüş et al., 2016), the Colorado Plateau (e.g., Levander et al., 2011), and the Betic-Rif region (e.g., Seber et al., 1996); yet a systematic examination and understanding of what happens after subduction termination is yet to be achieved.

Sabah, located in northern Borneo (Figures 1 and 2), represents a prime example of where post-subduction processes can be constrained. Indeed, northern Borneo has been the site

of two opposed subduction systems that ceased in the Late Miocene. The region exhibits a number of recent (after ~10 Ma, when the last subduction system stopped) and enigmatic features, including: subsidence followed by rapid uplift, exhumation of a subcontinental peridotite, localised intraplate volcanism, and emplacement of a magmatic pluton that subsequently emerged from mid-lower crustal depths to become the third highest peak in southeast Asia, Mt Kinabalu (4095 m).

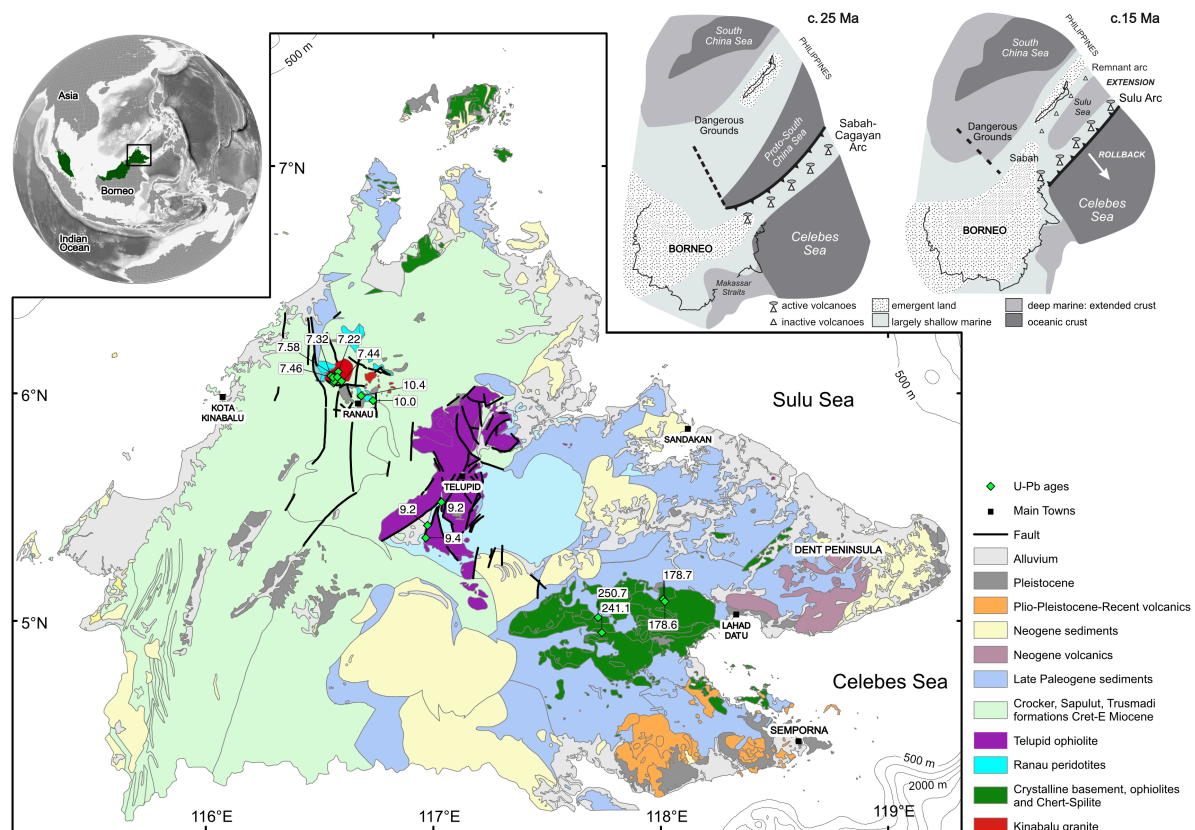


**Figure 1:** Geology map of Sabah. Green diamonds show the location of samples used for geochemical dating, with respective ages in Ma. Inset in the upper-left corner shows Malaysia in dark green and Sabah within the black rectangle. Inset in upper right corner summarizes the tectonic evolution of Borneo and the Sulu Sea in the late Paleogene and mid-Miocene (modified from Hall, 2013). Note that the two subduction systems (Proto-South China Sea and Celebes Sea) were sequential.

Several different models, often incompatible and conflicting, have been proposed to link surface observations with deeper structure in northern Borneo. However, they tend to be speculative due to a lack of direct geophysical observations of the lithosphere and underlying upper mantle. Previous tomographic models (e.g., Hall and Spakman, 2015; Zenonos et al., 2019) have insufficient spatial resolution (>250 km) to allow detailed inferences about crustal

and mantle processes to be made, although they appear to consistently illuminate a high-velocity anomaly centred beneath Sabah between ~50 and ~300 km depth. New and valuable insights into the evolution of northern Borneo were recently made by Pilia et al. (2021), with the primary suggestion that Sabah has undergone significant extension due to slab retreat in the Late Miocene, followed by the development of a Rayleigh-Taylor instability (Semporna Drip - SD) from a volcanic arc after subduction termination.

In this study, we use P and S relative arrival-time residuals to produce regional 3-D tomographic models of the lithosphere and underlying mantle, which may hold the key to understanding the mechanisms responsible for post-subduction processes in northern Borneo that could also be applied to similar settings globally. Our tomographic models are assessed and interpreted in terms of their ability to link mantle and surface processes that have occurred since the Neogene, hence making it possible to understand the influence of subduction termination on the lithosphere of northern Borneo.

## **2 Tectonic setting**

The older rocks of northern Borneo are exposed in eastern Sabah (near Lahad Datu), which form part of the Sabah ophiolite (Figure 1). Granites and metamorphic rocks of the crystalline basement were initially dated as Triassic (Leong, 1971), and these dates have been recently confirmed by modern U-Pb zircon dating (Burton-Johnson et al., 2020). The current tectonic framework of Sabah has been largely controlled by two opposing subduction systems. The older one is responsible for south-eastern subduction of the Proto-South China Sea (PSCS) beneath north-western Borneo between ca 40 and 20 Ma (Hall, 1996; Hutchison et al., 2000; Hall, 2013). Concurrent to the PSCS subduction is the deposition of the Trusmadi and Crocker Formations deep marine sediments in an older accretionary prism (Taylor and Hayes, 1983; Tongkul, 1991, 1994; Hutchison et al., 2000). These marine sediments were subsequently

deformed and elevated above sea level when the PCSC was entirely consumed in the mantle and continent-continent collision between the Dangerous Grounds block and north-western Borneo occurred. Subsequent north-west subduction of the Celebes Sea formed the Sulu Arc in the Dent and Semporna peninsulas (Figure 1), as indicated by calc-alkaline volcanism and K-Ar analysis (Rangin et al., 1990; Hall, 2013; Lai et al., 2021). Trench rollback of the Celebes Sea is likely to be responsible for back-arc extension and opening of the Sulu Sea (Hall, 2013), which is thought to have lasted from 21 to 9 Ma, consistent with the magmatic age compilation of Lai et al. (2021).

New zircon radiometric data from Tsikouras et al. (2021) have been used to demonstrate that Sulu Sea extension propagated into Sabah, suggesting that this process has led to exhumation, accompanied by uplift, of a subcontinental peridotite suite near Ranau and a rift-related magmatic episode (9.2-10.5 Ma) near Telupid. Following the termination of Celebes Sea subduction in the late Miocene, northern Borneo experienced several tectonic/geologic events that are difficult to reconcile with our current understanding of post-subduction tectonics. For instance, at the end of the Miocene eastern Sabah experienced a switch from subsidence to rapid and widespread uplift, making Sabah fully emergent in the early Pliocene (Balaguru & Nichols, 2004; Morley & Back, 2008). Furthermore, a granite pluton was emplaced at mid-lower crustal depths in a northwest-southeast extensional setting and crystallized between 7.8 and 7.2 Ma after intruding both peridotites and the Crocker Formation (Cottam et al., 2010, 2013), with zircon inheritance patterns implying melting of the underthrust continental crust of the Dangerous Grounds. Post-emplacement (~6-4.5 Ma) peak exhumation rates of more than 7 mm/yr have been found through low-temperature thermochronological data from the pluton (Cottam et al., 2013). Today, the pluton reaches an elevation of 4095 m (Figure 2) in the form of Mt Kinabalu, and towers over the Crocker Range (average height 1500 m) and most peaks in southeast Asia. Relatively recent loading of a fold-

and-thrust belt onto the attenuated Dangerous Ground crust resulted in a wide flexural depression offshore of Sabah to the west (Hall, 2013), a feature commonly misinterpreted as the relict PSCS trench location. Additionally, Plio-Pleistocene intraplate magmatism has been detected in the Semporna Peninsula, pointing to a change in mantle character from subduction-related volcanism to basaltic magmatism with an ocean island character (Macpherson et al., 2010).

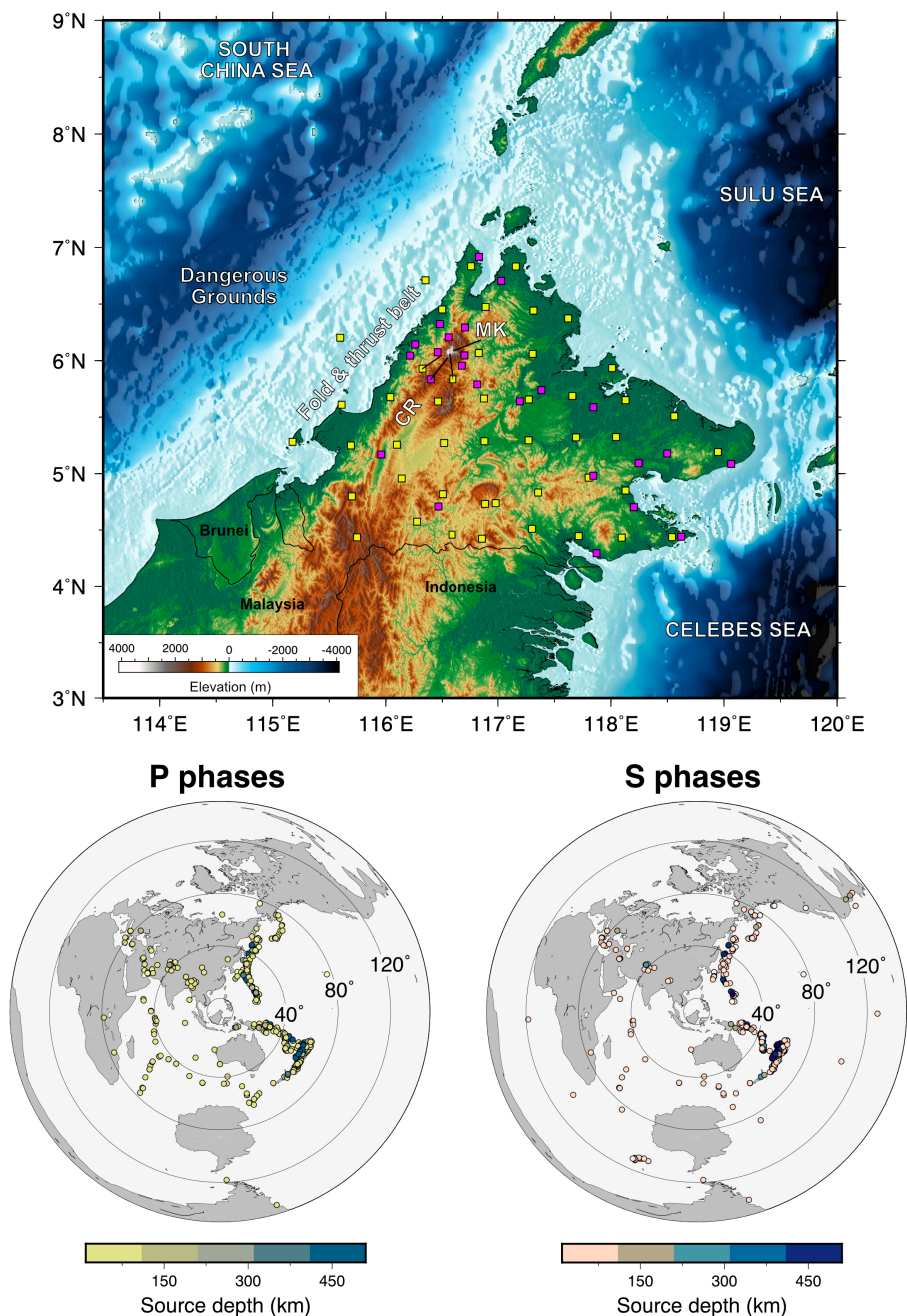


**Figure 2:** Topographic map of northern Borneo along with the location of the 46 temporary seismic stations from the nBOSS network (yellow squares) and 28 permanent stations of the seismic monitoring

network operated by the Meteorological Department of Malaysia (MetMalaysia, pink squares). The overall average station separation is 32 km. MK and CR denote the location of Mt Kinabalu and Crocker Range, respectively. Maps at the bottom show the distribution of teleseismic events used in this study to illuminate the 3-D P- and S-wave structure beneath the seismic network.

## 2 Data and methods

We use passive-seismic data collected by the northern Borneo Orogeny Seismic Survey (nBOSS - Pilia et al., 2019) network, which comprises 46 temporary seismic stations (Figure 2). Additional data is provided by 28 permanent stations of the seismic monitoring network maintained by the Meteorological Department of Malaysia (MetMalaysia). Our combined dataset includes arrival times from distant earthquakes recorded by 74 broadband seismic stations (32 km average station spacing) in the time window spanning from March 2018 to January 2020.

The data processing employed to extract relative arrival-time residuals is described in Pilia et al. (2020, 2021), therefore it is only briefly summarised here. Hypocentral parameters of the teleseismic events are selected from the International Seismological Centre catalogue, including any earthquake from any depth with  $m_b > 5$ , and an even lower threshold ( $m_b > 4.6$ ) if it occurred at a depth greater than 150 km. P waves are targeted and extracted from the vertical component of the continuous dataset, while horizontal components containing S wave information were rotated into radial and transverse components. Given the better quality of the radial component records, we discarded the transverse component data from subsequent analyses. While most of the arrival times are typically from first-arriving P- or S-waves, the addition of core and reflected phases (pP, Pdiff, PcP, PKiKP and sS, SKS, SKKS, SKiKS) allows us to use seismic sources from outside the typical epicentral distance window of  $27^\circ$ - $90^\circ$  used in teleseismic studies, thus permitting a wider range of incidence angles (Figure 2). Traces associated with the arrival of various global phases are windowed ( $\pm 60$  s) around the predicted arrival time, corrected for corresponding instrument responses and filtered between



0.05-4.0 Hz for P waves and 0.05-3.0 Hz for S waves with a Butterworth band-pass filter. Subsequently, for each source all traces are subject to preliminary alignment (Figure 3) using the global reference model ak135 (Kennett et al., 1995), and residual patterns across the network are obtained by exploiting the interstation coherency in P and S waveforms through an adaptive stacking technique (Rawlinson & Kennett, 2004). Relative arrival-time residuals and corresponding uncertainties are estimated after iteratively improving the alignment of each station trace with an initial reference trace, which is determined through stacking of all source-related traces. Examples of relative arrival time residual maps are shown in Figure 4 for both P and S waves. Sources retained for further processing are recorded by at least seven stations and have an average uncertainty estimate of the traveltime residuals that is less than 120 ms for P waves and 230 ms for S waves. Finally, the results of the stacking procedure are visually inspected to ensure consistency within each event region, and eliminate noisy or incoherent data.

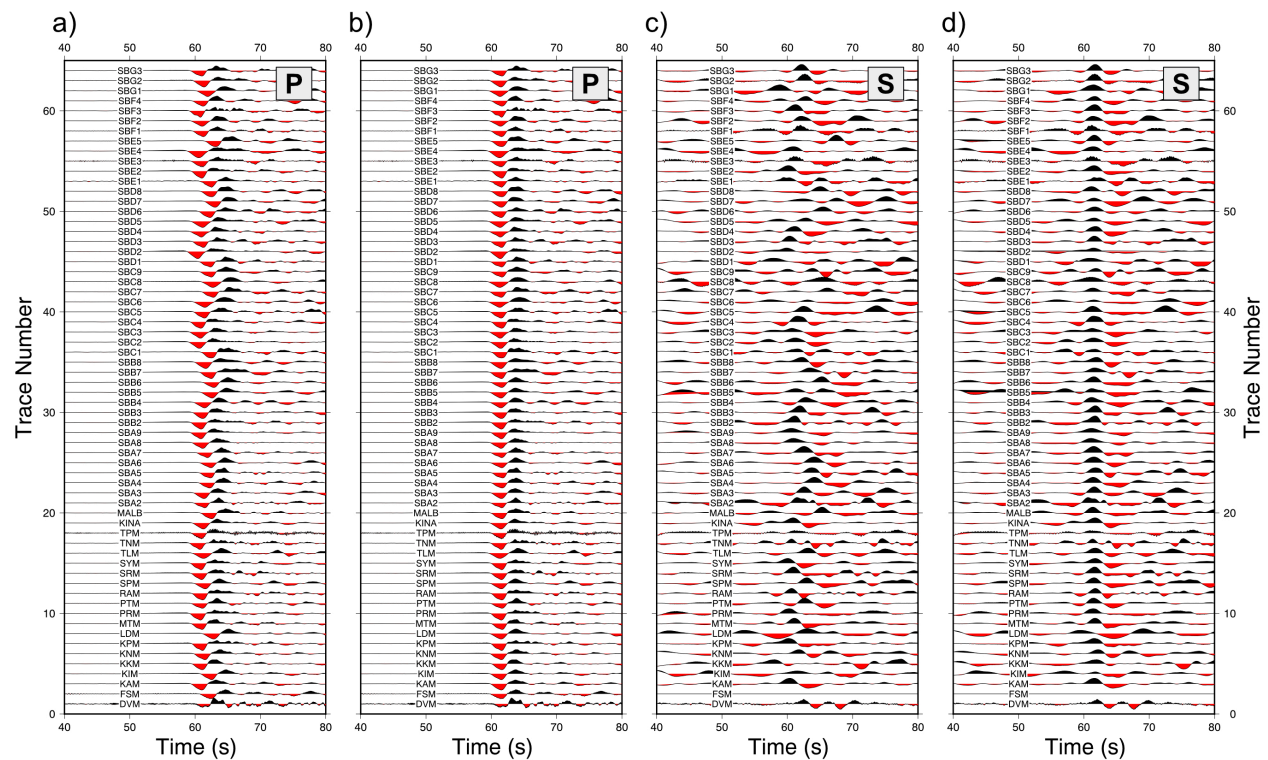


**Figure 3:** Records from the seismic stations used in this study from a teleseismic event that occurred in northern New Zealand on September 10, 2018. Initial alignment of the traces shown in a) and c) is obtained using the ak135 reference model. The apparent move-out of the traces can be attributed to



lateral variations in structure beneath the array. Final alignment shown in b) and d) is obtained after the application of the adaptive stacking technique. A map of the residuals for this specific event is illustrated in Figure 4.

Our final dataset comprised 32,300 residual times (ranging from -2.0 to 2.0 s) from 570 events for the P-wave dataset, and 13,723 residual times (ranging from -6.0 to 6.0 s) from 462 events for the S-wave dataset (Figure 2). P and S relative arrival-time residuals are independently inverted for 3-D velocity structure using the Fast-Marching tomographic code, FMTOMO (Rawlinson et al., 2006). FMTOMO is an iterative non-linear tomographic method that uses a grid-based eikonal solver known as the Fast-Marching Method (Sethian, 1999) to solve the forward problem of traveltime prediction through the laterally heterogeneous model volume. FMTOMO implements a subspace inversion scheme to solve the locally linearized problem at each iteration by matching observed and predicted traveltimes, subject to damping and smoothing regularization (Kennett et al., 1988).

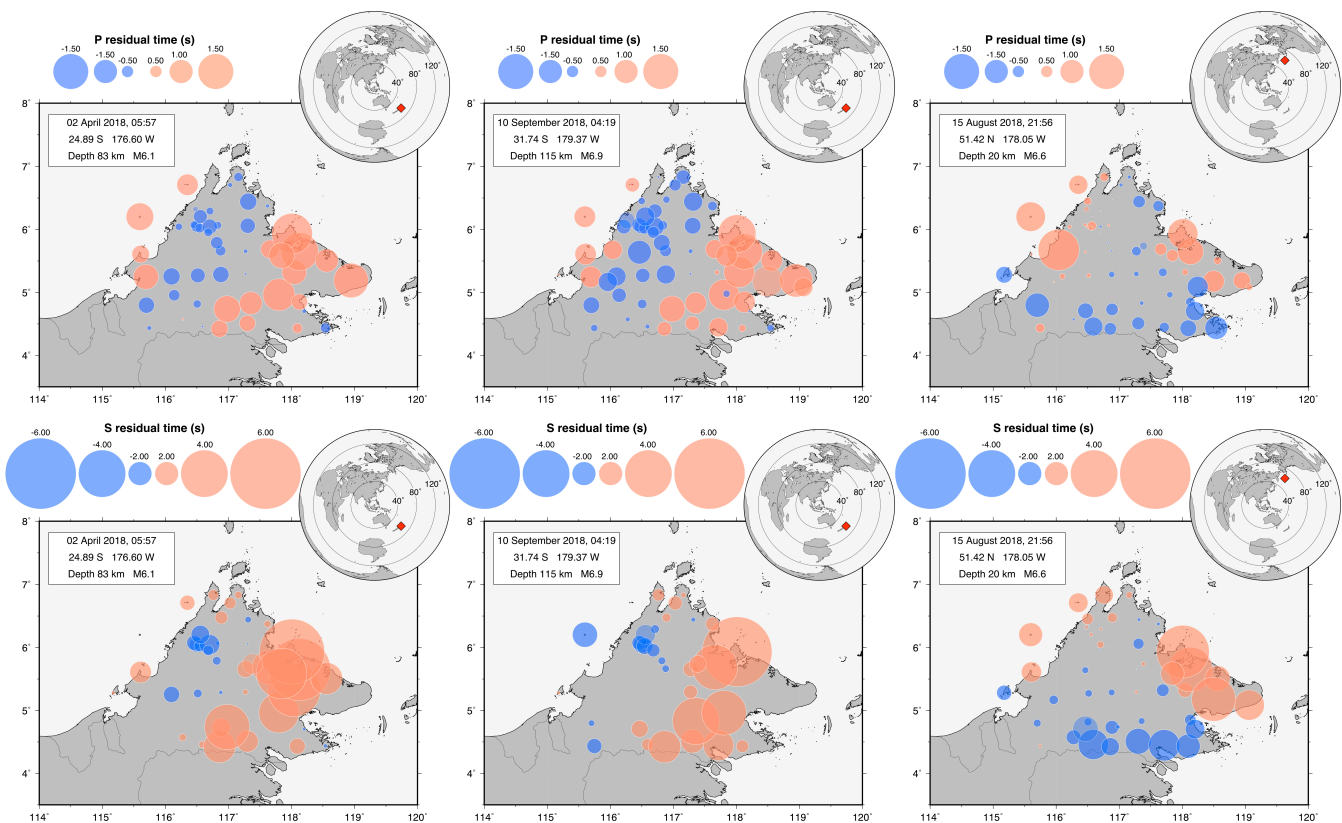


**Figure 4:** Pattern of relative arrival time residuals for P (upper panels) and S (lower panels) direct waves estimated using the adaptive stacking technique of Rawlinson & Kennett, 2004. The red diamond

in each map inset (top right corner) illustrates the location of the teleseismic source. Note how the polarity of the residuals for the same source is generally similar for both P and S waves, and for different sources with similar location. However, the arrival-time residual information is clearly dependent on the direction of the incoming rays; in fact, the pattern of residuals for sources located in northern New Zealand is different from that derived from sources located in Japan.

Pilia et al. (2021) have shown that lateral variations in Moho topography inferred using receiver function analyses can be up to 25 km in places with corresponding strong velocity heterogeneities in the crust, which are expected to significantly affect the pattern of arrival-time residuals. Therefore, to mitigate the effect of near-surface structural variations on the residual times that cannot be constrained by the teleseismic dataset (to depths roughly equal to the station spacing), crustal thickness variations and shear-wave velocities, determined from the joint inversion of receiver function and surface-wave dispersion, are directly included in FMTOMO as prior information (Rawlinson et al., 2016; Pilia et al., 2020). We use the relation of Brocher (2005), as implemented in, for example, Bodmer et al. (2018) and Pilia et al. (2020, 2021), to convert from crustal S-wave velocity to P-wave velocity. We decide to keep the Moho discontinuity fixed during the inversion, whereas crustal velocities are inverted for, given that teleseismic body waves cannot resolve the trade-off between velocity and interface depth, and the Moho geometry is likely better constrained by the receiver functions than crustal velocity. Similarly, station elevations are included in the forward calculation to account for differences in arrival time due to topographic variations.

## **3 Results**

### ***3.1 Resolution tests***

The recovery of synthetic structure is a common strategy utilized in seismic tomographic experiments to assess the resolution and reliability of tomographic images. Here, this is achieved by following recommendations of Rawlinson and Spakman (2016). This involves recovering a sparse distribution of spikes (Figure 5), and synthetic structures that resemble those recovered in the final solution model (sufficiently different to avoid the issue

of preconditioning – Figures 6 and 7). All synthetic arrival-time residuals are generated using an identical source-receiver combination and phase types as the observed dataset. For any given synthetic 3-D structure, rays are predicted through the known structure. Subsequently, Gaussian random noise is added to the resulting arrival-time residuals to simulate the picking uncertainty associated with the real data (standard deviation of 0.1 and 0.2 sec for P and S residual times, respectively). The same inversion scheme used with the observational dataset, along with parameterization and initial velocity model, is eventually used to recover the P and S synthetic structures. A direct comparison between the recovered structures and predetermined input anomalies makes it possible to assess the spatial resolution and reliability of the features illuminated with the field data, typically dependent on path coverage and data noise.

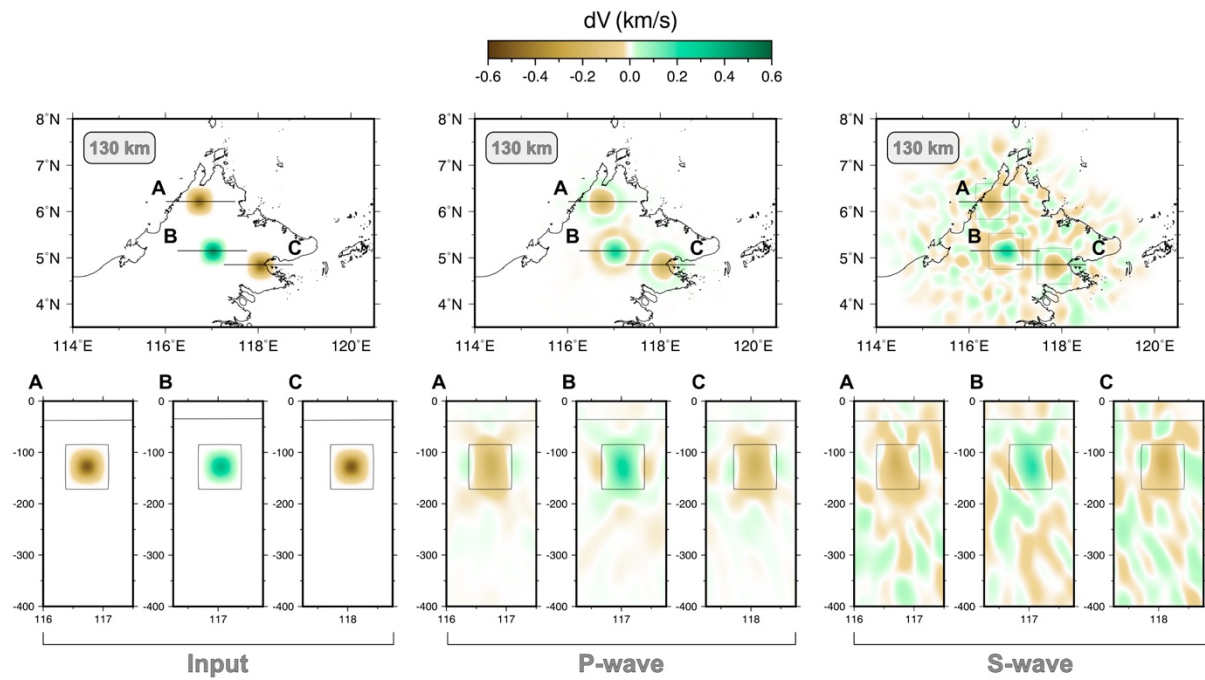


**Figure 5:** Resolution test based on synthetic structures involving three spikes with maximum amplitude of -0.6 dV and 0.6 dV for negative and positive spikes, respectively. A, B and C show the location of the spikes in horizontal view (top panels) and vertical view (bottom panels). High and low velocity heterogeneities outside the recovered target structures are largely a function of the random noise that is added to the synthetic data.

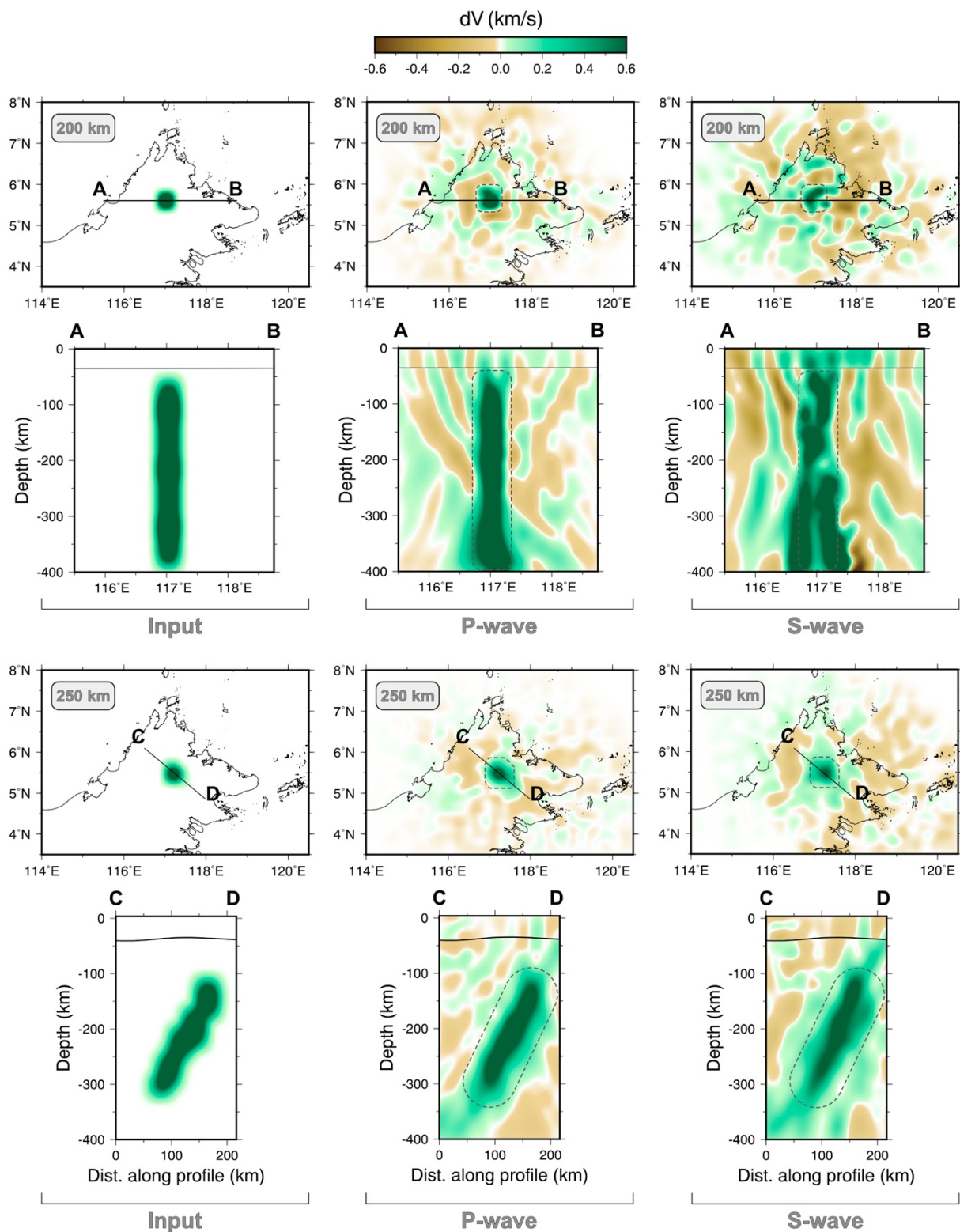
The first test we conduct is shown in Figure 5, which involves a series of relatively short-wavelength structures to verify the effects of smearing. Two low-velocity spikes (-0.6

km/s velocity perturbation) are located in the Ranau area and close to the Semporna peninsula, while a high velocity spike (0.6 km/s velocity perturbation) is located in south-central Sabah. The three input spikes are generally well identified, preserving the location and polarity as per the input model, without exhibiting apparent directionally dependent smearing. Nonetheless, as is common when comparing P and S tomographic models, smearing is far more pronounced and anomalies are smoother in S-wave velocity models, predominantly due to the poorer data coverage and less accurately picked S residual times (see Figure S1).

The second set of tests is designed to examine the capability of our dataset and inversion method to recover synthetic structure that mimic those observed with the field dataset. The first experiment includes a roughly cylindrical high velocity perturbation that is vertical (profiles AB and 200 km depth in Figure 6) and tilted (profiles CD and 250 km depth in Figure 6). The input structures are accurately recovered for both the vertical and tilted P- and S-wave anomalies. Smearing of the S-wave reconstructions is evident in places, particularly in profile AB (250-400 km depth) and CD (150-400 km depth at model distance 150-210 km). It is also important to note how the tilted anomaly in plan view (250 km depth in the S-wave model) is smeared out over a relatively large area, likely due to imposition of smoothing regularisation.

The goal of the last synthetic test is to assess whether we can recover two high-velocity synthetic slabs with opposite dip: one along the north-western coastline of Sabah dipping to the southeast, and another in central Sabah dipping to the northwest. The former would be expected by the presence of a PSCS slab (A in Figure 7), while the latter is used to test whether our dataset would be able to image a potential Celebes Sea slab (B in Figure 7) in central Sabah. The recovered models suggest that slab B can be faithfully recovered with both P and S residual times if present in the observational dataset. Similarly, slab A can be recovered with a high degree of confidence, even if its offshore extent can be affected by substantial smearing due to

272 the sparse raypath coverage in this part of the study area, which needs to be taken into  
 273 consideration when interpreting the final 3-D tomographic model (see Figure S1).



274 **Figure 6:** Resolution test based on synthetic structures involving a vertical (profile A to B) and tilted  
 275 (profile C to D) high-velocity anomaly, with respective horizontal slices at 200 and 250 km. High  
 276

and low velocity heterogeneities outside the recovered target structures are largely a function of the random noise that is added to the synthetic data.

Overall, our recovered synthetic structures demonstrate that our dataset and tomographic approach are appropriate to robustly detect a range of different anomalies in the upper mantle beneath Sabah, although the recovered S-wave anomalies appear to be smoother and more prone to artifacts than the P-wave anomalies. This is common in tomographic experiments, since the number and quality of S-wave residuals tend to be lower than their P-wave counterpart.

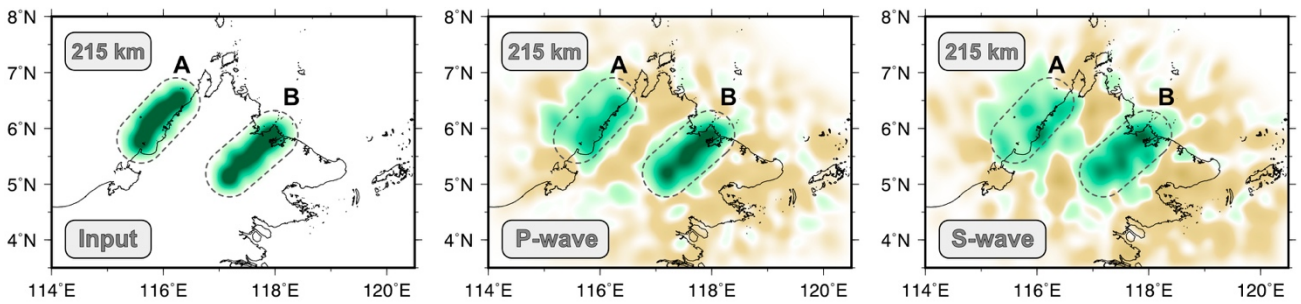
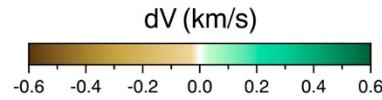


**Figure 7:** Horizontal slices through the synthetic slab recovery test. A and B indicate the location of two synthetic slabs. High and low velocity heterogeneities outside the recovered target structures are largely a function of the random noise that is added to the synthetic data.

### 3.2 $V_p$ and $V_s$ tomographic solution models

We define a local 3-D region for the inversion of P- and S-wave arrival-time residuals that spans a latitude range of 3.5° to 8° N, a longitude range of 114° to 120.5° E, and a depth range of 3.7 above sea level to 400 km below sea level. The 3-D inversion volume is parametrised through a regular 3-D grid of nodes, which constitute cubic B-spline volume elements used to create a smoothly varying, locally controlled velocity field. The inversion grid spacing is equal to ~15 km in all directions, resulting in a total of 39,104 unknowns. The

forward step is performed on a propagation grid that is defined by  $\sim 10$  km node spacing in all directions, totalling 141,120 nodes. The complete tomographic procedure is accomplished by iteratively running the forward and inversion calculations through six iterations to produce a final tomographic solution model. Damping and smoothing regularizations are used after being systematically determined by evaluating the trade-off curves between data misfit, model smoothness, and model variance (see Figure S2). Considering the relatively large range of arrival-time residuals, we decide to perform a first-pass tomographic inversion, which is then repeated upon removal from the datasets of the source-receiver combinations resulting in the largest residual times ( $\pm 1.5$  s for P phases and  $\pm 4$  s for S phases). The data variance is reduced by 87% and 67% in the  $V_p$  and  $V_s$  tomographic models, respectively (see histograms in Figure 8). The final data misfit is evaluated from the difference between the observed and predicted traveltime residuals, the latter being calculated relative to an initial model containing only the ak135 reference model and with all receivers set at zero elevation (as per the adaptive stacking approach from which residuals are initially computed).

We present our  $V_p$  and  $V_s$  final tomographic models via a series of horizontal slices at 100 km depth intervals (Figure 8), along with four vertical sections (Figure 9). Generally, most of the large-scale features that we interpret in the next section appear common to both  $V_p$  and  $V_s$  models, although with varying geometries and amplitude in places, presumably due, at least in part, to the poorer resolution of the  $V_s$  model. For example, a major positive velocity perturbation dominates the lower part of our tomographic models beneath profile A (Figure 9). While this feature is well-defined in our  $V_p$  tomographic model, it does seem to be affected by a degree of vertical smearing in the  $V_s$  model. A depth slice taken at 300 km depth from the  $V_p$  model indicates that this is a prominent feature with elevated wavespeeds and a strike approximately parallel to that of the Crocker range. This anomaly is supported by the synthetic test results in Figure 7, which reveal that the level of smearing is negligible around this feature,



except perhaps in its offshore extent. Two vertical profiles across this anomaly (profiles C and D in Figure 9) confirms that elevated wavespeeds are located roughly beneath the Crocker range and extend from about 225 km depth to the bottom of the tomographic model, with a thickness of ~75 km. As previously anticipated, this high-velocity perturbation is detectable in the respective depth slice and vertical profiles of the  $V_s$  model, albeit with a somewhat lower resolution.

Another major feature emerges from profiles B and D in Figure 9. In particular, profile D exhibits a subvertical, positive perturbation of both P and S wave velocity extending from roughly the location of Plio-Pleistocene lava from the Semporna Peninsula to the neighbourhood of Telupid. The amplitude and angle of this anomaly is strongly supported by the synthetic test results, which show that we can recover the anomaly with confidence, although the  $V_s$  model experiences a greater degree of vertical smearing.

## **4 Discussion**

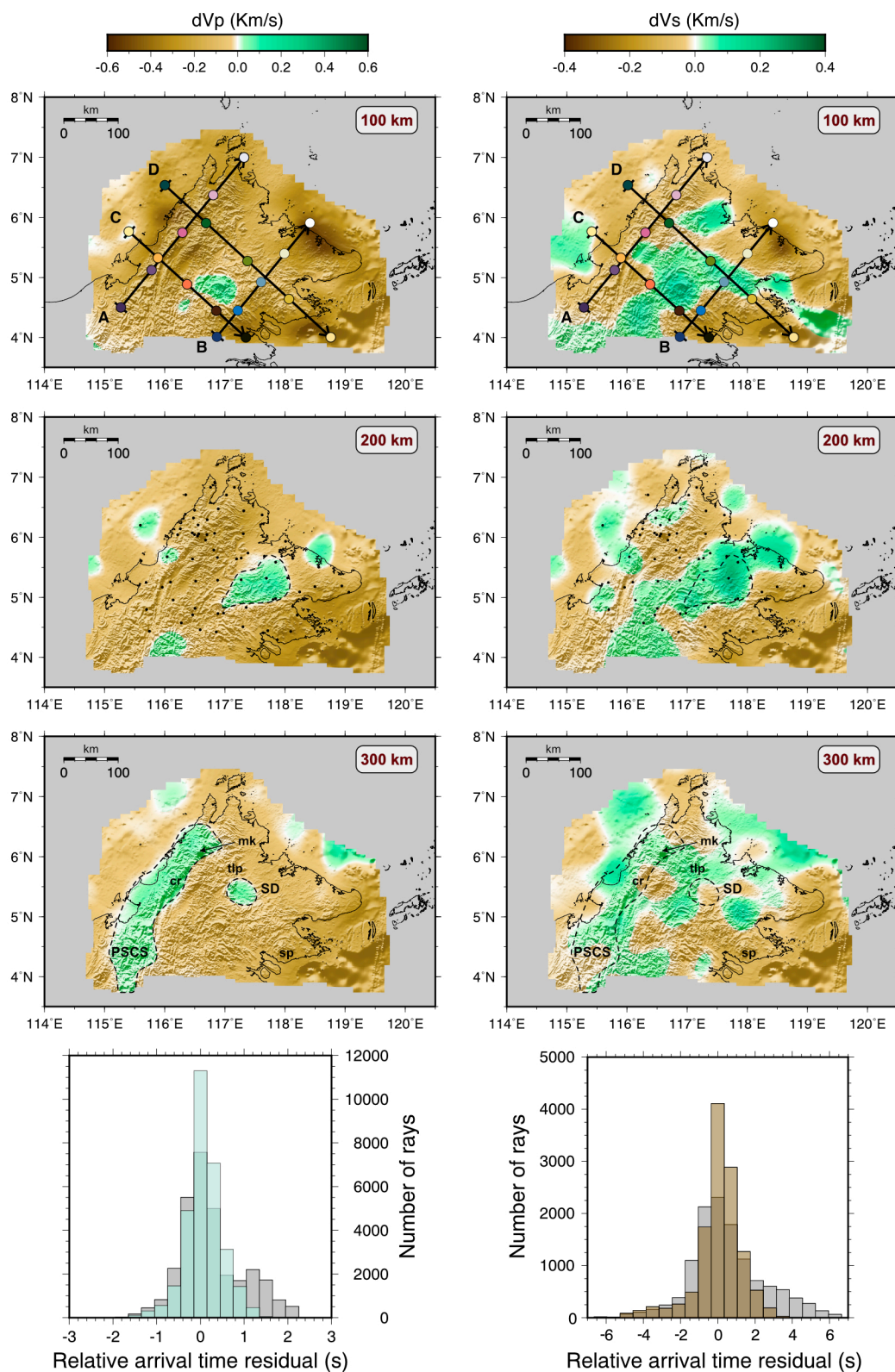
### ***4.1 Remnant of the PSCS slab or lithospheric delamination?***

In both Figure 8 (300 km slice) and Figure 9 (profiles A, C, and D) a distinct high-velocity region of P and S wavespeeds can be observed in westernmost Sabah, terminating to the north around an area where the topography exhibits a sudden change in strike of approximately 90°, and possibly continuing to the south beyond our seismic network. This could be either a remnant of the PSCS slab, or the signature of delaminated lower lithosphere (Bird, 1979) beneath the Crocker Range. To evaluate these two hypotheses, we analyse the seismic images in tandem with other available information.

Removal of negatively buoyant parts of the lithosphere is typically accompanied by a trend of subsidence at the onset of delamination followed by isostatic adjustment (i.e., uplift), lower crustal (if included in the removal process) or lithospheric thinning with consequent asthenospheric upwelling and basaltic magmatism at the surface (e.g., Göğüş and Ueda, 2018).



350 Several lines of evidence suggest Neogene (23 – 2.5 Ma) uplift of 0.3 mm/yr in the Crocker  
 351 Range (Morley & Back, 2008).



352  
 353 **Figure 8:** Horizontal slices extracted from the final tomographic  $V_p$  and  $V_s$  models at 100, 200  
 354 and 300 km depth. Profiles A, B, C and D in the depth slices at 100 km indicate the location of

the vertical profiles shown in Figure 10. Black dots in the depth slices at 200 km denote the seismic stations used in this study. Histograms show the distribution of relative arrival-time residuals for the initial models (grey) and the final solution models (aqua for the  $V_p$  model and brown for the  $V_s$  model). The average of both P-wave and S-wave arrival-time residuals is zero. SD: Semporna Drip; PSCS: Proto-South China Sea; mk: Mt Kinabalu; cr: Crocker Range; sp: Semporna Peninsula; tlp: Telupid.

Direct evidence of crustal and/or lithospheric thinning beneath the Crocker Range is lacking. Pilia et al. (2021) derived a crustal thickness map of Sabah using P-to-S conversion at the Moho by analysing receiver functions, revealing a relatively thick crust of up to 55 km in the region beneath the Crocker Range (Figure 10), a product of the collision between the attenuated lithosphere of the Dangerous Grounds and western Sabah. Furthermore, Pilia et al. (2021) and Greenfield et al. (2022) demonstrate that the lithosphere in this region is not particularly thin, with an average thickness of 110 km. The high-velocity feature imaged in our tomography model shows a body at least 150 km long in the vertical direction; while this can be overestimated due to the vertical smearing inherent to teleseismic tomography studies, we demonstrate that such an effect is not significant in our resolution tests (Figure 5), at least for the P-wave model. Thus, justifying a pre-delamination lithospheric thickness of more than 200 km (present day thickness plus that of the high velocity anomaly) would be difficult. Evidence of possible asthenospheric upwelling is not conspicuous either; meaningful low velocity anomalies, suggestive of likely hot mantle temperatures, are not manifested in our tomographic images beneath the orogenic belt, particularly in the S-wave model, which is more sensitive to temperature variations.

Associating the high-velocity perturbation beneath the Crocker Range to the PSCS is a more viable solution, although not devoid of issues. Problems with this interpretation stem from the location and geometry of the anomaly. First, Mt Kinabalu contains zircons that indicate a contribution to the melt of old continental crust (Cottam et al., 2010, 2013), which is interpreted as extended continental crust of the Dangerous Grounds underthrust during Early

Miocene collision. For this reason, a possible slab of the PSCS would be expected to be further to the southeast with respect to the present-day location. Second, most of the PSCS is thought to be now in the lower mantle (Hall and Spakman, 2015). For these reasons, we postulate that we are likely to illuminate an upper-mantle remnant of the PSCS (Figure 10). It is plausible that when the subduction rate decreased due to the buoyancy effect of the continental lithosphere entering the subduction region, this effect imparted a steep angle to the high-velocity anomaly we observe today. This latter process may have led to slab-detachment at the continent-ocean transition due to its own weight, which can occur even 10 Ma after onset of continental collision (Duretz et al., 2011; Magni et al., 2013), and may be the explanation for the recent uplift in western Sabah as calculated by Morley & Back (2008). Subsequent or concurrent plate motion to the southeast (the present absolute plate motion is 2.7 cm/yr) can explain why the PSCS slab remnant is not found further to the east.

#### ***4.2 Lithospheric foundering in Semporna***

An oceanic slab of the Celebes Sea beneath Borneo or the Sulu Sea has never been imaged using geophysical methods; however, a well-developed volcanic arc (Sulu Arc) extending from Dent and Semporna peninsula into the Philippines is an unambiguous indicator of a past subduction system. Despite demonstrating with our resolution tests that our dataset would be able to image a hypothetical high-velocity slab beneath eastern Sabah (Figure 7), our final solution models (Figures 8 and 9) do not manifest evidence for such a slab. This observation leads to the obvious question as to where the Celebes Sea slab is today.

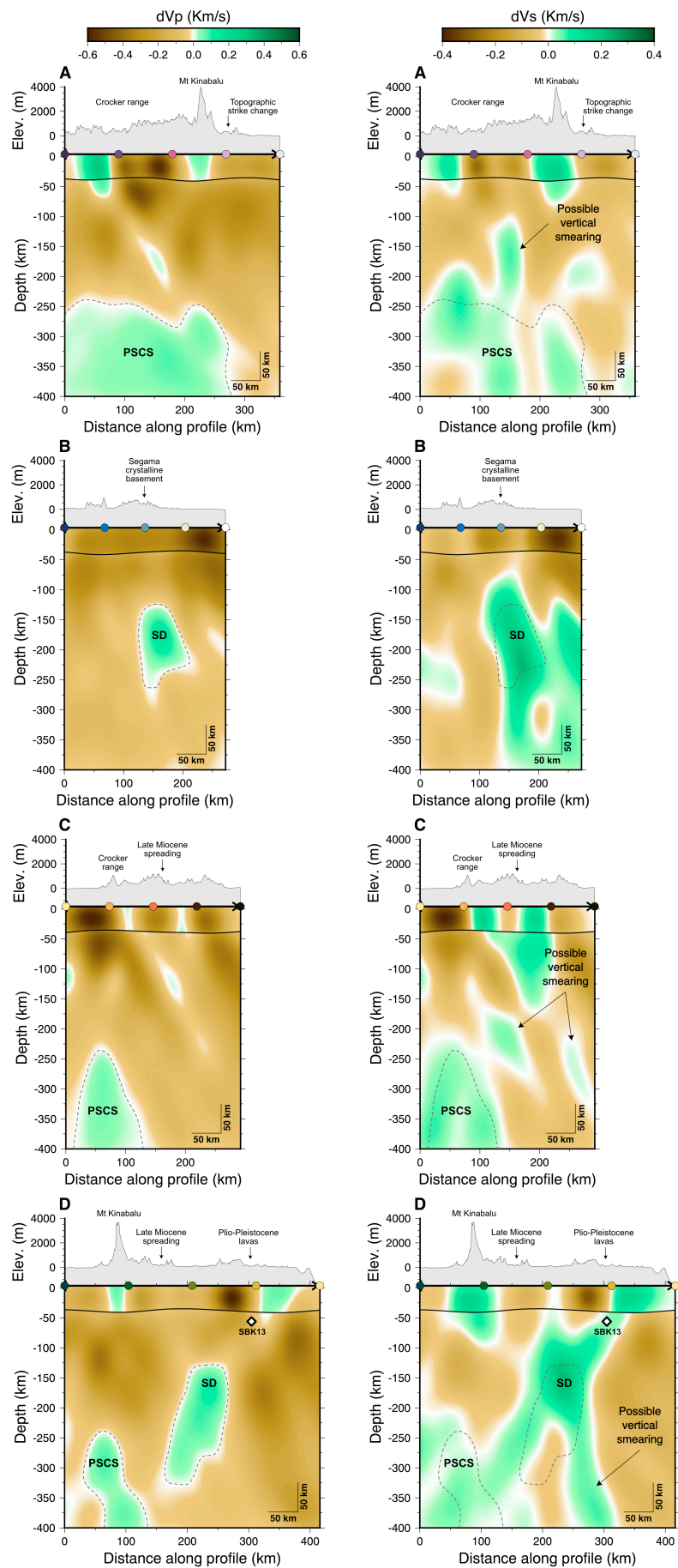


**Figure 9:** Vertical slices extracted from the final tomographic  $V_p$  and  $V_s$  models (see Figure 8 for location). White diamond in profile D denotes the approximate location of sample SBK13. Gray dashed lines highlight the main P-wave velocity anomaly discussed in the text. SD: Semporna Drip; PSCS: Proto-South China Sea.

A distinct seismically fast perturbation in eastern Sabah is visible in the P-wave tomographic model, and is somewhat confirmed by the S-wave model (SD in Figure 8 and 9), which is contaminated by lateral and vertical smearing as indicated by our resolution tests (Figures 5 and 6). Pilia et al. (2021) interpreted this anomaly as a dripping Rayleigh-Taylor instability developed from the Sulu Arc root. Additional evidence supporting foundering of dense lower lithosphere in Semporna include: i) subsidence (starting at ~14 Ma with widespread sedimentation) followed by rapid uplift in eastern Sabah (Balaguru, & Nichols, 2004), ii) Plio-Pleistocene intraplate volcanism in Semporna (Macpherson et al., 2010), iii) evidence for thin lithosphere beneath Semporna from the estimated melting depth of basalts (sample SBK13 from Macpherson et al. (2010) – see Figures 9 and 10 for location) and seismic imaging methods (Pilia et al., 2021; Greenfield et al., 2022). A set of similar observations has been made for western California, where interpretation of the seismically fast Isabella anomaly has long been attributed to either lithospheric downwelling or a fossil slab (Zandt et al., 2004; Pikser et al., 2012). However, a recent interpretation by Dougherty et al. (2021) favours a fossil slab origin, since they claim that seismic imaging reveals a connection between a high-velocity perturbation located in the upper mantle with the surface extension of the Monterey microplate in the offshore. However, we believe that there is no justification for advocating a fossil slab analogy between the Isabella anomaly and Semporna drip in the eastern part of northern Borneo. First, albeit our tomographic models do not extend far enough into the Celebes Sea, a connection between the SD and the present-day oceanic lithosphere of the Celebes Sea is geometrically not obvious. Second, Pilia et al. (2021) have shown that the dip of the SD can be dynamically reproduced with a prescribed plate velocity of 4 cm/yr (relative motion between

surface plate and underlying mantle) in about 10 Ma, which is approximately the time since Celebes Sea subduction has stopped and downwelling of dense material begun. This is also the time needed for the anomaly to reach a depth of around 400 km and translate horizontally by 170 km from the location of the Sulu Arc to its present-day location (distance between the near-surface departure of the drip and its base at 400 km depth). Post-subduction foundering in the form of a lithospheric drip is therefore our favoured explanation (Figure 10). Any remnants from the subduction of the Celebes Sea remain to be seismically imaged. Currently, its location could well be outside of our seismic network, perhaps being too deep (>400 km) or further to the east. Cessation of subduction and the approximately coeval onset of Celebes Sea subduction in northern Sulawesi may have played a role in disguising the seismic signature and/or location of the Celebes Sea slab.

#### ***4.3 A link between surface and deep observations in a post-subduction setting***

The integration of our tomographic results with structural mapping and geochronology information enables us to constrain the Neogene post-tectonic evolution of northern Borneo. Our model develops the idea that two diachronous, opposed subducting systems were active in northern Borneo since the Paleogene. Following subduction termination of the PSCS, underthrusting of the Dangerous Ground block beneath western Sabah elevated the Crocker Range and significantly thickened the crust. A remnant of the PSCS (Figure 10) is now located in the upper mantle but it is unclear whether full or partial detachment from the continental lithosphere has occurred. The 4-8 km uplift of the Crocker Range during the Late-Miocene-Pliocene can be explained by invoking this detachment. Collision, uplift and crustal thickening precipitated a tectonic mode-switch to orogen collapse since 2 Ma, as indicated by recent GPS analysis (Sapin et al., 2013).

Slab rollback of the Celebes Sea induced widespread extension in central Sabah (Hall, 2013), as inferred from crustal-thickness estimates (Figure 10), exhumation of a subcontinental peridotite near Ranau, and a magmatic rifting episode in central northern Borneo (Tsikouras et al., 2021). Our detailed tomographic images of the upper mantle beneath northern Borneo illuminate an unusually small lithospheric drip, which has been modelled by Pilia et al. (2021) to deliver insights into the dynamic evolution of Sabah since the Late Miocene. Lithospheric foundering is approximately coeval to subduction termination of the Celebes Sea, and developed from a dense gravitational instability beneath the Sulu Arc. The SD contribution to extension near Telupid and Ranau is unclear but it is likely to have played a role. Pilia et al. (2021) have shown that removal of the lithosphere from the Sulu Arc may have caused significant extension in the Ranau and Kinabalu area. As a result of this phase of northwest-southeast directed extension, the crust beneath Kinabalu was considerably stretched, thereby reducing the isotherm depth and triggering melting of the lower crust, which ultimately emplaced the Kinabalu pluton. The density-dependent isostatic rebound of the granitic rocks of Mount Kinabalu could explain their rapid exhumation and uplift (Braun et al., 2014). Our results imply that the SD is currently detached from the lithosphere and sinking into the asthenospheric mantle; a direct consequence of lithospheric removal is asthenospheric upwelling, which can be invoked to account for the distribution of recent volcanism in Semporna Peninsula. The topographic response associated with lithospheric removal is also intimately connected to the evolution of the drip, resulting in subsidence during the accumulation of dense material at the base of the lithosphere, to subsequent isostatic rebound (e.g., uplift) during lithospheric removal. We suggest that the evidence for this type of mechanism is preserved in the stratigraphic record of eastern Sabah, exhibiting a switch from subsidence (and sedimentation) to topographic uplift.



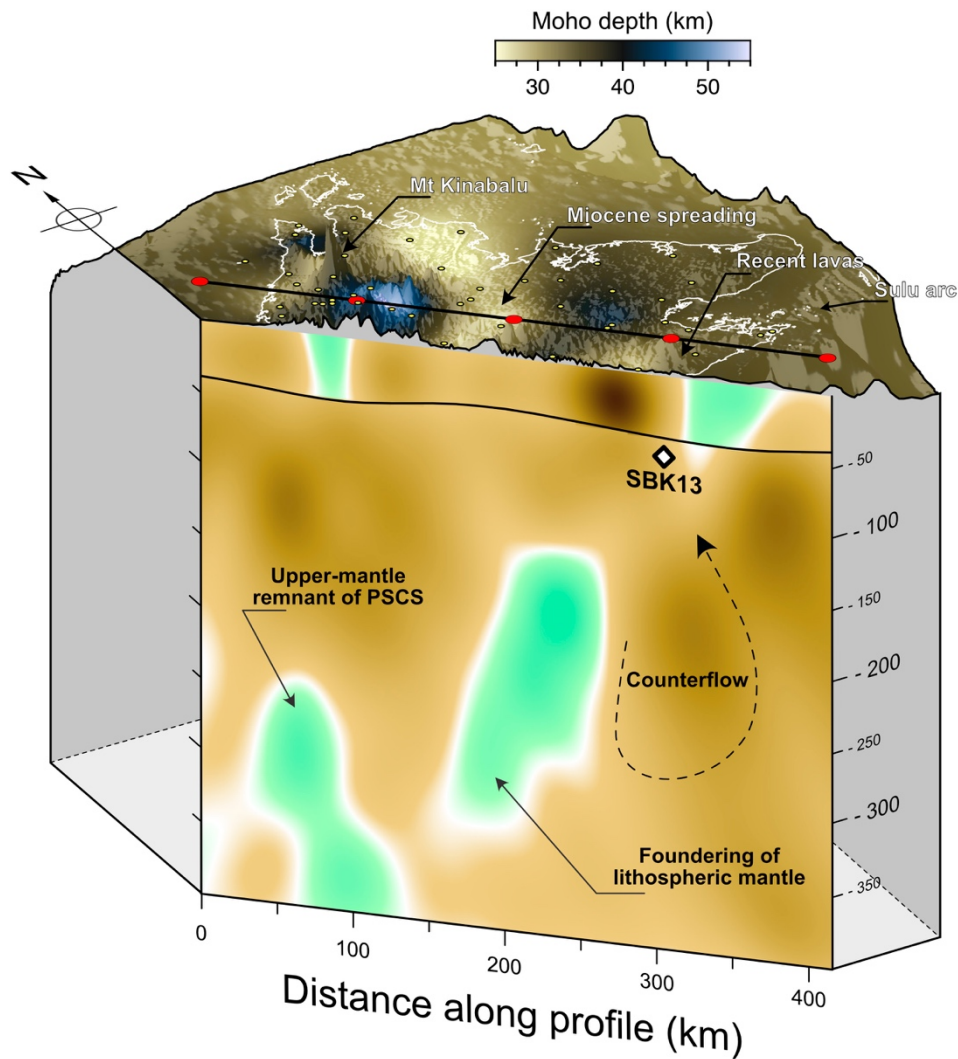


**Figure 10:** Schematic illustration of the findings from this study. Tomographic transect is the same as Figure 9D (P wavespeed). Note the intentional horizontal gap on the surface between the location of the transect (black line and red dots) and that of the tomographic profile. The tomographic profile does not extend into the Celebes Sea. The white line is the coastline superimposed on elevation color-shaded by crustal thickness (from Pilia et al., 2021). Yellow dots are seismic stations.

## Conclusions

We have used P and S teleseismic arrival times to construct 3-D tomographic models of the lithosphere and underlying upper mantle beneath northern Borneo. The two tomographic models show a compelling degree of consistency, although the S-wave model is more prone to vertical and lateral smearing, an expected effect due to the typical lower quality of the S-wave arrivals and poorer coverage. Our 3-D models reveal that a slab remnant of the PSCS is present



beneath northern Borneo, implying that tectonic reconstructions of SE Asia that preclude southeast oriented subduction of the PSCS are hard to justify in light of this new evidence. Another significant finding of this study is the presence of a surprisingly small lithospheric drip that possibly developed from the volcanic root of the Sulu Arc after subduction termination. We infer that despite its size, the drip is directly or indirectly responsible for most of the observations and surface features that distinguish northern Borneo. Such phenomena may therefore play a more important role in shaping continental margins than previously thought.

## **Acknowledgments**

S.P. acknowledges support from the Natural Environmental Research Council (NERC) Grant NE/R013500/1 and from the European Union's Horizon 2020 Research and Innovation Program under Marie Skłodowska-Curie Grant Agreement 790203. We thank the TanDEM-X Science Communication Team (German Aerospace Center (DLR) e.V.) for providing TanDEM topographic data. We thank the NERC Geophysical Equipment Facility for loan 1038 and seismometers loaned by the University of Cambridge and Aberdeen.

## References

- Balaguru, A. & Nichols, G., 2004. Tertiary stratigraphy and basin evolution, southern Sabah (Malaysian Borneo). *J. Asian Earth Sci.*, **23**, 537-554.
- Bird, P., 1979. Continental delamination and the Colorado Plateau. *Journal of Geophysical Research: Solid Earth*, **84**, pp.7561-7571.
- Bodmer, M., Toomey, D.R., Hooft, E.E. and Schmandt, B., 2018. Buoyant asthenosphere beneath Cascadia influences megathrust segmentation. *Geophysical Research Letters*, **45**, 6954-6962.
- Braun, J., Simon-Labric, T., Murray, K.E. and Reiners, P.W., 2014. Topographic relief driven by variations in surface rock density. *Nature Geoscience*, **7**, 534-540.
- Brocher, T.M., 2005. Empirical relations between elastic wavespeeds and density in the Earth's crust. *Bulletin of the seismological Society of America*, **95**, 2081-2092.
- Burton-Johnson, A., et al., 2020. A Triassic to Jurassic arc in north Borneo: Geochronology, geochemistry, and genesis of the Segama Valley Felsic Intrusions and the Sabah ophiolite. *Gondwana Res.*, **84**, 229-244.
- Clark, M.K., Maheo, G., Saleeby, J. and Farley, K.A., 2005. The non-equilibrium landscape of the southern Sierra Nevada, California. *GSA Today*, **15**, 4.
- Cottam, M., Hall, R., Sperber, C. & Armstrong, R., 2010. Pulsed emplacement of the Mount Kinabalu granite, northern Borneo. *J. Geol. Soc.*, **167**, 49-60.
- Cottam, M.A., Hall, R., Sperber, C., Kohn, B.P., Forster, M.A. and Batt, G.E., 2013. Neogene rock uplift and erosion in northern Borneo: evidence from the Kinabalu granite, Mount Kinabalu. *J. Geol. Soc.*, **170**, 805-816.
- Dougherty, S.L., Jiang, C., Clayton, R.W., Schmandt, B. and Hansen, S.M., 2021. Seismic evidence for a fossil slab origin for the Isabella anomaly. *Geophysical Journal International*, **224**, 1188-1196.

536 Ducea, M.N. and Saleeby, J.B., 1996. Buoyancy sources for a large, unrooted mountain  
537 range, the Sierra Nevada, California: Evidence from xenolith thermobarometry. *Journal of*  
538 *Geophysical Research: Solid Earth*, **101**, 8229-8244.

539 Duretz, T., Gerya, T.V. and May, D.A., 2011. Numerical modelling of spontaneous slab  
540 breakoff and subsequent topographic response. *Tectonophysics*, **502**, 244-256.

541 Evans, J.R., Achauer, U., 1993. Teleseismic velocity tomography using the ACH  
542 method: theory and application to continental-scale studies. In: Iyer, H.M. and Hirahara, K.  
543 (Eds.), *Seismic Tomography: Theory and Practice*, **13**, 319-360.

544 Göğüş, O.H., Pysklywec, R.N. and Faccenna, C., 2016. Postcollisional lithospheric  
545 evolution of the Southeast Carpathians: Comparison of geodynamical models and  
546 observations. *Tectonics*, **35**, 1205-1224.

547 Göğüş, O.H. and Ueda, K., 2018. Peeling back the lithosphere: Controlling parameters,  
548 surface expressions and the future directions in delamination modeling. *Journal of*  
549 *Geodynamics*, **117**, pp.21-40.

550 Hall, R., 1996. Reconstructing Cenozoic SE Asia. *Geol. Soc. Spec. Publ.* **106**, 153-184.

551 Hall, R., 2013. Contraction and extension in northern Borneo driven by subduction  
552 rollback. *J. Asian Earth Sci.*, **76**, 399-411.

553 Hall, R. and Spakman, W., 2015. Mantle structure and tectonic history of SE  
554 Asia. *Tectonophysics*, **658**, 14-45.

555 Hutchison, C.S., Bergman, S.C., Swauger, D.A. and Graves, J.E., 2000. A Miocene  
556 collisional belt in north Borneo: uplift mechanism and isostatic adjustment quantified by  
557 thermochronology. *Journal of the Geological Society*, *157*(4), 783-793.

558 Jacobson, G., 1970. Gunong Kinabalu Area, Sabah, Malaysia. *Geol. Surv. Malaysia*  
559 *Rept.*, **8**, 111.

Kennett, B. L. N., M. S. Sambridge, and P. R. Williamson (1988). Subspace Methods for Large Inverse Problems with Multiple Parameter Classes. *Geophys. J. Int.* **94**, 237-247.

Kennett, B. L. N., Engdahl, E. R., and Buland, R., (1995). Constraints on seismic velocities in the Earth from traveltimes. *Geophys. J. Int.* **122**, 108-124.

Lai, C.K., Xia, X.P., Hall, R., Meffre, S., Tsikouras, B., Rosana Balangue-Tarriela, M.I., Idrus, A., Ifandi, E. and Norazme, N.A., 2021. Cenozoic Evolution of the Sulu Sea Arc-Basin System: An Overview. *Tectonics*, **40**, p.e2020TC006630.

Leong, K.M., 1971. Peridotite-gabbro problems, with special reference to the Segama Valley and Darvel Bar areas, Sabah, East Malaysia. *Warta Geologi* 28, 4-13.

Levander, A., Schmandt, B., Miller, M.S., Liu, K., Karlstrom, K.E., Crow, R.S., Lee, C.T. and Humphreys, E.D., 2011. Continuing Colorado plateau uplift by delamination-style convective lithospheric downwelling. *Nature*, **472**, 461-465.

Macpherson, C.G., Chiang, K.K., Hall, R., Nowell, G.M., Castillo, P.R. and Thirlwall, M.F, 2010. Plio-Pleistocene intra-plate magmatism from the southern Sulu Arc, Semporna peninsula, Sabah, Borneo: Implications for high-Nb basalt in subduction zones. *J. Volcanol. Geotherm. Res.*, **190**, 25-38.

Magni, V., Faccenna, C., van Hunen, J. and Funiciello, F., 2013. Delamination vs. break-off: the fate of continental collision. *Geophys. Res. Lett.*, **40**, 285-289.

Morley, C.K. & Back, S., 2008. Estimating hinterland exhumation from late orogenic basin volume, NW Borneo. *J. Geol. Soc.*, **165**, 353-366.

Pilia, S., Rawlinson, N., Gilligan, A. and Tongkul, F., 2019. Deciphering the fate of plunging tectonic plates in Borneo. *Eos, Transactions American Geophysical Union*, **100**, 18-23.

583 Pilia, S., Hu, H., Ali, M.Y., Rawlinson, N. and Ruan, A., 2020. Upper mantle structure  
 584 of the northeastern Arabian Platform from teleseismic body-wave tomography. *Physics of the*  
 585 *Earth and Planetary Interiors*, **307**, <https://doi.org/10.1016/j.pepi.2020.106549>.  
 586 Pilia, S., Davies, D. R., Hall, R., Bacon, C., Gilligan, A., Greenfield, T., et al., 2021.  
 587 Effects of post-subduction processes on continental lithosphere.  
 588 <https://doi.org/10.21203/rs.3.rs-861968/v1>  
 589 Pikser, J.E., Forsyth, D.W. and Hirth, G., 2012. Along-strike translation of a fossil  
 590 slab. *Earth and Planetary Science Letters*, **331**, 315-321.  
 591 Raikes, S.A., 1980. Regional variations in upper mantle structure beneath southern  
 592 California. *Geophysical Journal International*, **63**, 187-216.  
 593 Rangin, C., Bellon, H., Benard, F., Letouzey, J., Muller, C. and Sanudin, T. (1990).  
 594 Neogene arc-continent collision in Sabah, northern Borneo (Malaysia). *Tectonophysics*, **183**,  
 595 305-319.  
 596 Rawlinson, N., Kennett, B. L. N., 2004. Rapid estimation of relative and absolute delay  
 597 times across a network by adaptive stacking. *Geophys. J. Int.*, **157**, 332-340.  
 598 Rawlinson, N., de Kool, M., Sambridge, M., (2006). Seismic wavefront tracking in 3-  
 599 D heterogeneous media: applications with multiple data classes. *Explor. Geophys.*, **37**, 322-  
 600 330.  
 601 Rawlinson, N. and Spakman, W., 2016. On the use of sensitivity tests in seismic  
 602 tomography. *Geophysical Journal International*, **205**, 1221-1243.  
 603 Rawlinson, N., Pilia, S., Young, M., Salmon, M. and Yang, Y., 2016. Crust and upper  
 604 mantle structure beneath southeast Australia from ambient noise and teleseismic  
 605 tomography. *Tectonophysics*, **689**, 143-156.

- Sapin, F., Hermawan, I., Pubellier, M., Vigny, C. and Ringenbach, J.C., 2013. The recent convergence on the NW Borneo Wedge - a crustal-scale gravity gliding evidenced from GPS. *Geophysical Journal International*, **193**, 549-556.
- Sethian, J. A. (1999), Fast Marching Methods, *SIAM Review*, *41*(2), 199-235, doi:10.1137/s0036144598347059.
- Seber, D., Barazangi, M., Ibenbrahim, A. and Demnati, A., 1996. Geophysical evidence for lithospheric delamination beneath the Alboran Sea and Rif-Betic mountains. *Nature*, **379**, 785-790.
- Taylor, B. and Hayes, D.E., 1983. Origin and history of the South China Sea basin. In: Hayes, D. E. (Ed.), *The tectonic and geologic evolution of Southeast Asian seas and islands: Part 2*. American Geophysical Union, vol. 27. Geophysical Monographs Series, 23-56.
- Tongkul, F., 1991. Tectonic evolution of Sabah, Malaysia. *Journal of Southeast Asian Earth Sciences*, **6**, 395-405.
- Tongkul, F., 1994. The geology of Northern Sabah, Malaysia: its relationship to the opening of the South China Sea Basin. *Tectonophysics*, *235*(1-2), pp.131-147.
- Wernicke, B., Clayton, R., Ducea, M., Jones, C.H., Park, S., Ruppert, S., Saleeby, J., Snow, J.K., Squires, L., Fliedner, M. and Jiracek, G., 1996. Origin of high mountains in the continents: The southern Sierra Nevada. *Science*, **271**, 190-193.
- Zandt, G., Gilbert, H., Owens, T.J., Ducea, M., Saleeby, J. and Jones, C.H., 2004. Active foundering of a continental arc root beneath the southern Sierra Nevada in California. *Nature*, **431**, 41-46.
- Zenonos, A., De Siena, L., Widiyantoro, S. and Rawlinson, N., 2019. P and S wave travel time tomography of the SE Asia-Australia collision zone. *Physics of the Earth and Planetary Interiors*, **293**, 106267.

## **Data and software availability**

Waveform data from the nBOSS network will be publicly accessible through the IRIS Data Management (<http://www.iris.edu/mda>) from February 2023 (see for details [https://doi.org/10.7914/SN/YC\\_2018](https://doi.org/10.7914/SN/YC_2018)). Details on the status of this database may be obtained from N.R. Access to waveform data from the Malaysian national network (<https://www.fdsn.org/networks/detail/MY/>) is restricted. The final P- and S-wave tomographic models can be downloaded from the following digital object identifier <https://doi.org/10.6084/m9.figshare.19583722.v1>.

The source code for the Adaptive Stacking method used to compute the arrival time residuals is available at <http://www.earth.edu.au/codes/AdaptiveStacking/>. The source code and manual for FMTOMO are available at <http://earth.edu.au/codes/FMTOMO/>.

# Supplementary Material for

## **Seismic signature of subduction termination from teleseismic P- and S-wave arrival-time tomography: the case of northern Borneo**

Pilia S., Rawlinson N., Hall R., Cornwell D.G., Gilligan A., Tongkul F.

Correspondence to: [simone.pilia@unimib.it](mailto:simone.pilia@unimib.it)

This file includes:

Figs S1 to S2



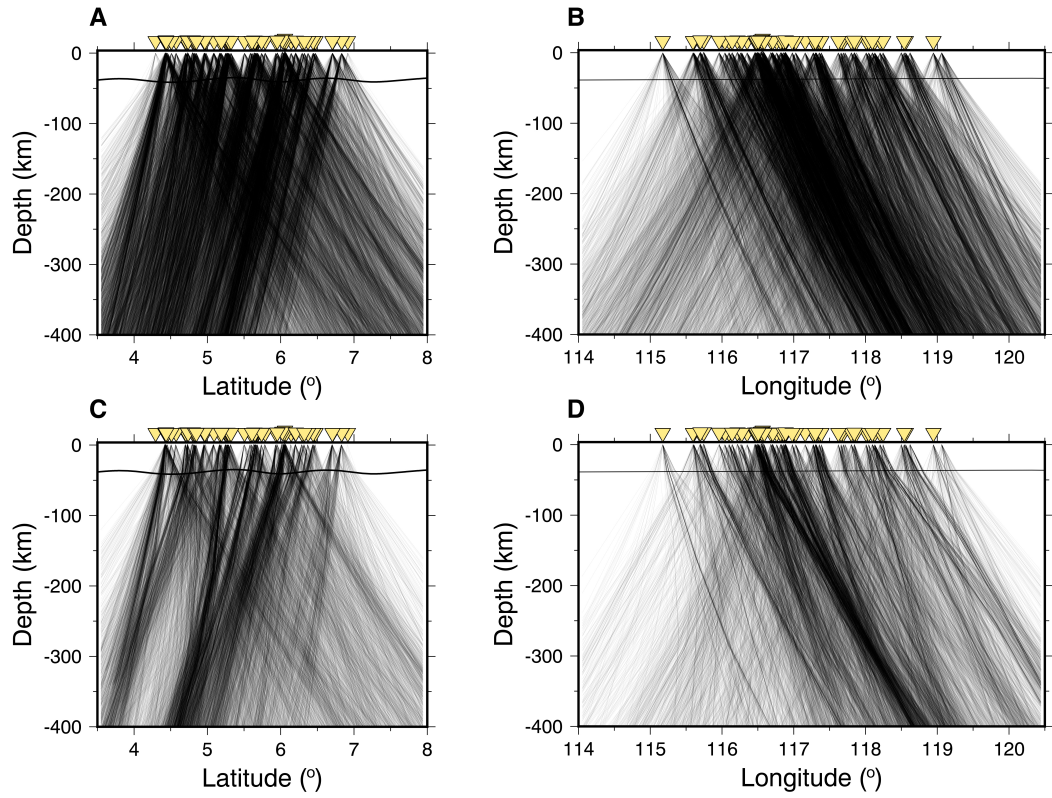


**Figure S1:** Raypath coverage beneath the study area. Rays are projected onto a N-S profile (A and C for P- and S-wave arrivals, respectively) taken at longitude  $117^{\circ}\text{E}$ , and one E-W profile (B and D for P- and S-wave arrivals, respectively) taken at latitude  $5^{\circ}\text{N}$ . Note that the plots show one ray every sixty. Inverted light-yellow triangles illustrate the projection of all stations.

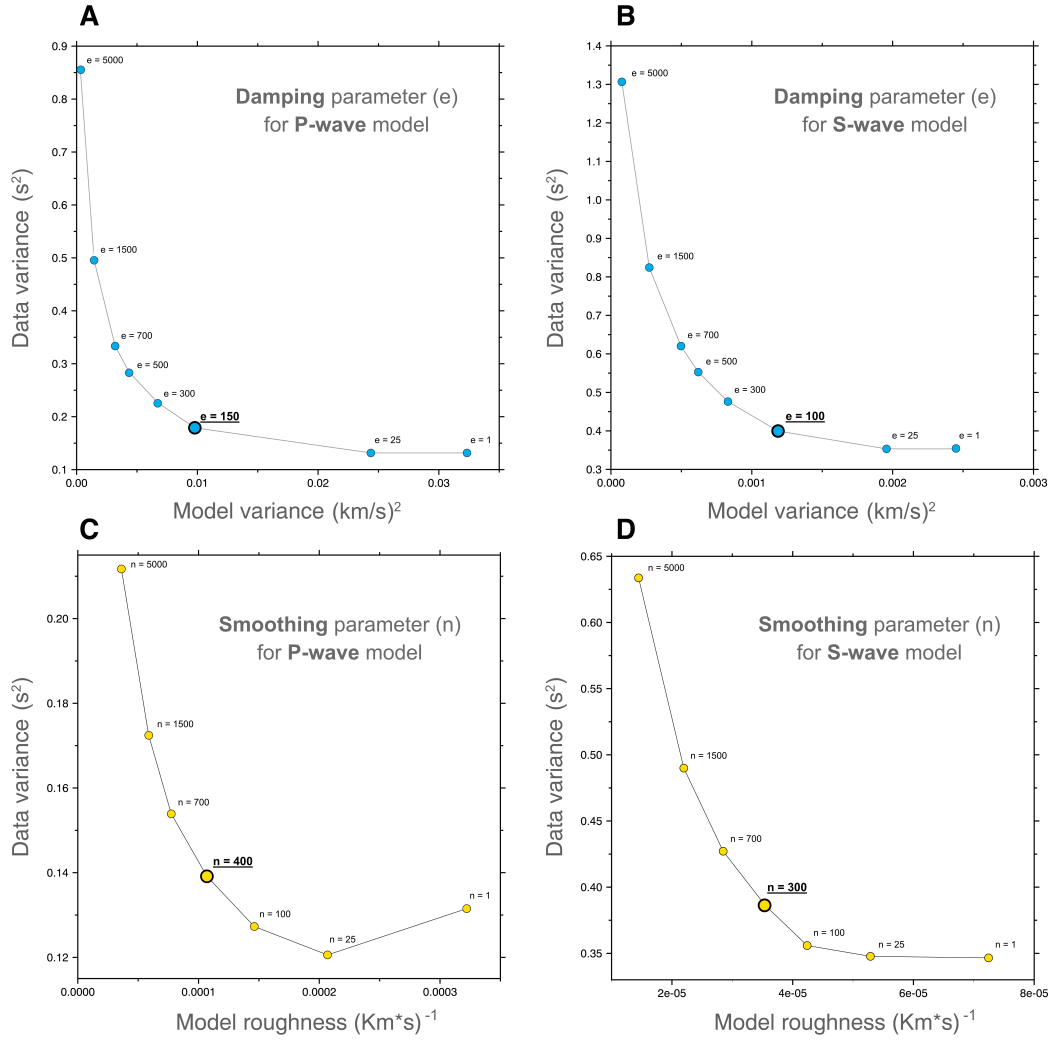


**Figure S2:** Trade-off curves between data variance and model variance to evaluate the damping factor for the P-wave (A) and S-wave (B) tomographic model. Trade-off curves between data variance and model roughness to evaluate the smoothing factor for the P-wave (C) and S-wave (D) tomographic model.